Nonlinear Quantum Photonics With AlGaAs Bragg-Reflection Waveguides

Félicien Appas, Othmane Meskine, Aristide Lemaître, Martina Morassi, Florent Baboux, Maria. I. Amanti, and Sara Ducci

(Invited Paper)

***Abstract*—Integrated photonics is playing a key role in the development of quantum technologies covering applications ranging from quantum communication to computing and from simulations to sensing. In this context, material platforms enabling the chip-scale integration of quantum components are a key issue on the way towards real-world and large-scale technological implementations. In this paper, we review our last achievements on AlGaAs Bragg reflection waveguides emitting nonclassical states of light by spontaneous parametric down conversion. The choice of this platform combines the advantages of a mature fabrication technology, room temperature operation, emission in the telecom C-Band and compliance with electrical injection. We demonstrate the ability of these devices to generate a large variety of quantum states spanning from biphoton frequency combs to broadband polarization entanglement enabling promising applications in quantum processing as well as flexible quantum networks.**

***Index Terms*—Entanglement, integrated photonics, photon-pair sources, quantum communications, quantum networks, quantum optics.**

I. Introduction

INTEGRATED quantum photonics is a rapidly growing research field at the intersection between integrated photonics and quantum technologies. Indeed, the ability to generate, manipulate, and detect quantum states of light plays an essential role in all areas of quantum technologies including quantum communications, computing, simulation, and metrology: either directly exploiting quantum properties of photons, or indirectly, using photons as a carrier of information probing and/or interacting with quantum states of other quantum systems. In the same way as for classical photonics, the chip-scale integration of quantum components has become essential to move from laboratory demonstrations to large-scale implementation and real-world technologies. To this aim, a variety of material platforms are actively investigated, including Lithium Niobate, Silicon-based materials, and III-V semiconductors. Table I summarizes the optical and optoelectronic properties of some of the main platforms used to develop nonlinear quantum photonic devices [1], [2]. Among semiconductors, GaAs and related compounds such as AlGaAs are the most extensively investigated and developed since they combine several crucial assets [3], [4]. GaAs is transparent from 1 μm to 10 μm; strong mode confinement can be realized thanks to a high refractive index (3.2 at 1.5 μm). Quantum states of light can be generated either by embedded quantum dots or via nonlinear optical effects [2]. Indeed, GaAs displays one of the highest second order nonlinearity with respect to commonly used platforms ($d_{36} \approx 170\,\mathrm{pm/V}$ at 1550 nm), as well as a high Kerr coefficient ($n_2 \approx 1.6 \times 10^{-17}\ \mathrm{m^2\,W^{-1}}$ at 1550 nm), therefore both spontaneous parametric down conversion (SPDC) and spontaneous four wave mixing (SFWM) can be used to generate photon pairs. We note that, differently from Silicon-On-Insulator which is plagued by two-photon absorption, an appropriate choice of Al content allows to get rid of this issue in AlGaAs devices. Moreover, the platform presents a direct bandgap, opening the way to the monolithic integration of laser diodes into quantum photonic chips, as well as a high electro-optic coefficient ($r_{14} \approx 1.4 \times 10^{-12}\ \mathrm{m/V}$) [5], enabling ultrafast on-chip manipulation of single and two-photon states [6]. Very recently, thanks to the efforts made to reduce its optical losses, AlGaAsOI has made its entry as a material platform for the development of nonlinear quantum photonic devices [7], [8]. So far, the generation of photon pairs by SFWM has been demonstrated using the third order nonlinearity [9], [10], and the development of quantum photonic components is in progress. In contrast, this work focuses on the generation of quantum states of light by SPDC using second order nonlinearity in AlGaAs ridge waveguides. Different phase-matching (momentum conservation) schemes have been implemented to achieve efficient nonlinear frequency conversion processes [2], [11], among which we can mention form birefringence, obtained via selective oxidation of AlAs

Manuscript received 11 June 2022; revised 5 September 2022 and 8 October 2022; accepted 10 October 2022. Date of publication 13 October 2022; date of current version 16 December 2022. The work of Othmane Meskine was supported by Labex Science and Engineering for Advanced Materials and devices (SEAM) under Grants ANR-10-LABX-0096 and ANR-18-IDEX-0001. This work was supported in part by Agence Nationale de la Recherche (ANR) through the QUANTIFY Project under Grant ANR-19-ASTR-0018-01, in part by the French RENATECH Network, and in part by Paris Ile-de-France Région in the framework of DIM SIRTEQ through the Project Paris QCI and Project LION. *(Corresponding author: Sara Ducci.)*

Félicien Appas, Othmane Meskine, Florent Baboux, Maria. I. Amanti, and Sara Ducci are with the Université Paris Cité, CNRS, Laboratoire Matériaux et Phénomènes Quantiques, 75013 Paris, France (e-mail: felicien.appas@icfo.net; othmane.meskine@u-paris.fr; florent.baboux@u-paris.fr; maria.amanti@u-paris.fr; sara.ducci@u-paris.fr).

Aristide Lemaître and Martina Morassi are with the Center for Nanosciences and Nanotechnologies, Université Paris Saclay/CNRS, 91120 Palaiseau, France (e-mail: aristide.lemaitre@c2n.upsaclay.fr; martina.morassi@c2n.upsaclay.fr).

Color versions of one or more figures in this article are available at https://doi.org/10.1109/JLT.2022.3214466.

Digital Object Identifier 10.1109/JLT.2022.3214466

TABLE I
MAIN NONLINEAR PLATFORMS FOR INTEGRATED QUANTUM PHOTONICS

	Nonlinearity	Linear losses (dB/cm)	Two-photon absorption (C-band)	Index contrast	Electrical pumping	Electro-optic modulation
Lithium Niobate (LN) [25]	$\chi^{(2)}$	0.1 (C-Band)	—	low	—	Pockels (GHz speed)
Lithium Niobate on Insulator (LNOI) [26]	$\chi^{(2)}$	0.03 (NIR)	—	high	—	Pockels (GHz speed)
Silicon on Insulator (SOI) [27]	$\chi^{(3)}$	0.45 (C-Band)	high	high	—	Free-carrier injection (GHz speed)
Silica on Silicon (SoS) [28, 29]	$\chi^{(3)}$	5×10^{-4} (1580 nm)	moderate	low	—	—
Silicon Nitride (SiN) [30]	$\chi^{(3)}$	$< 10^{-2}$ (C-Band)	—	moderate	—	Electrostatic or up to MHz speed
AlGaAs [24]	$\chi^{(2)}, \chi^{(3)}$	0.4 (C-Band)	—	moderate	Yes	Pockels (GHz speed)
AlGaAs on Insulator (AlGaAsOI) [9]	$\chi^{(2)}, \chi^{(3)}$	0.3 (C-Band)	—	high	Yes	Pockels (GHz speed)

layers within the heterostructure [12], counterpropagating phase matching in a transverse pump configuration [13], and modal phase matching in a collinear geometry [14]. The first solution is based on a three-wave interaction among fundamental modes : this results in a high nonlinear overlap integral having led to optical parametric oscillation [15], but optical losses at the interfaces of the oxidized layers hinders its utilization for quantum optics applications. The counterpropagating phase matching scheme leads to the generation of relatively narrowband biphoton states ($\approx 0.1\,nm$) and is particularly interesting for its versatility in frequency correlation and exchange statistics engineering [16], [17]. Lastly, modal phase matching in a colinear geometry can be employed to generate broadband biphoton states. By tailoring the waveguide design, broadband polarization entangled photons can be emitted directly at the chip output, a particularly appealing property for wavelength-multiplexed quantum networks applications. In this scheme, the phase-velocity mismatch is compensated by a multimode waveguide dispersion engineering. The three interacting modes can either be confined by homogeneous claddings [14] or by using Bragg reflectors; the latter option, proposed and analyzed in [18], has been adapted to AlGaAs waveguides in [19], allowing to increase the versatility in the dispersion engineering while reducing the total aluminum content. Different epitaxial designs have been proposed and/or been implemented by several groups depending on the specific target application [4], [20], [21], [22], [23]. In the following, we present a review on the generation of quantum states of light through SPDC in colinear modal phase matching with the AlGaAs Bragg reflection waveguides developed in our group. The results presented in this work have been obtained with samples pumped with an external laser, but the design we have adopted for these devices is compliant with the monolithic integration of an electrically driven laser diode together with the nonlinear waveguide working at room temperature [24], a crucial feature for the development of real-world quantum photonic circuits.

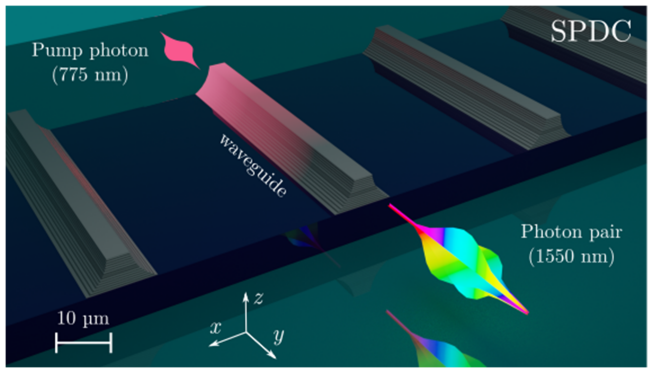

Fig. 1. Artist view depicting the SPDC process used to generate photon pairs with Bragg reflection waveguides. A near-infrared pump photon coming either from an external laser, as represented here, or from an on-chip III-V laser diode, is downconverted into a pair of telecom photons through modal phase-matching.

II. WORKING PRINCIPLE OF THE DEVICE

A. Device Design

The working principle of the nonlinear integrated AlGaAs photon-pair source is sketched in Fig. 1. A pump beam around 775 nm is coupled into the AlGaAs waveguide and generates, by SPDC, photon pairs in the telecom band.

The devices are fabricated by etching a ridge waveguide from an AlGaAs wafer consisting of a stacking of $Al_xGa_{1-x}As$ layers with varying Al concentration x, grown on a $[001]$ GaAs substrate by molecular beam epitaxy. A core layer made of $Al_{0.45}Ga_{0.55}As$ is sandwiched between two Bragg mirrors consisting of alternating 116 nm-thick $Al_{0.25}Ga_{0.75}As$ layers and 280 nm-thick $Al_{0.2}Ga_{0.8}As$ layers. These mirrors provide both a photonic band gap confinement for multilobes 'Bragg' modes around 775 nm and total internal reflection confinement for fundamental modes in the telecom band. Details on the design of the Bragg reflectors can be found in Refs. [18], [31], [32]. The waveguides are typically 1 to 3 mm-long with a ridge width of 2 to 7 μm and typical etching depth defined either slightly above the core (for active devices or for photonic circuits based on evanescent coupling) or all the way down to the substrate (for simple ridge waveguides) (see Fig. 3).

The SPDC process follows the usual energy and momentum conservation conditions (the latter also called phase-matching), that are mathematically written as

$$\omega_p = \omega_1 + \omega_2 \tag{1}$$

$$n_p(\omega_p)\omega_p = n_1(\omega_1)\omega_1 + n_2(\omega_2)\omega_2, \tag{2}$$

where ω_p is the frequency of the pump photon and ω_1, ω_2 that of the downconverted photons, while n_p, n_1, n_2 denote the effective mode indices of the three interacting modes. The first condition (1) requires to be in the transparency range of the material; the second one (2) requires to engineer the effective refractive index of the interacting modes (and thus the epitaxial

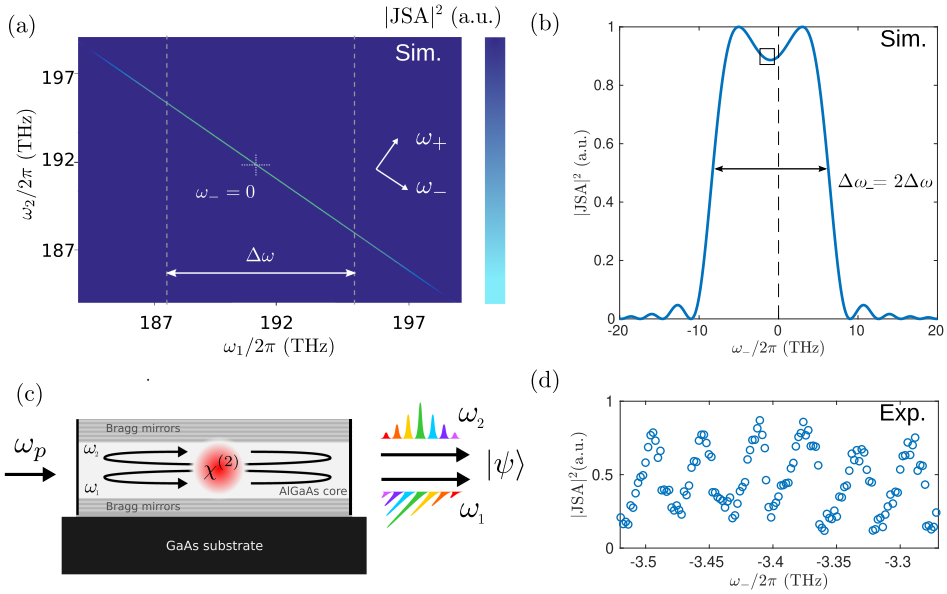

Fig. 2. (a) Simulated joint spectral intensity (JSI) corresponding to the modulus squared of the JSA. For the sake of visualization, the pump bandwidth value in this simulation has been set to 10GHz, instead of 100kHz as in the experiment reported in this paper. (b) Corresponding antidiagonal profile $|f_-(\omega_-)|^2$ of the JSI. (c) Sketch illustrating the generation of biphoton frequency combs using a nonlinear AlGaAs waveguide (figure from Ref. [34]). (d) Experimental reconstruction by stimulated emission tomography of a portion of the antidiagonal profile of the JSI exhibiting discrete resonance peaks arising from the cavity effects due to the waveguide facets.

structure and waveguide geometry). At the same time, the conversion efficiency of the device is maximized by optimizing the nonlinear overlap integral of the three interacting fields and the material nonlinearity.

In these devices, three types of phase-matching schemes can be achieved: 1) Type 0, where the pump photon and the downconverted photons are all TM-polarized; this process is made possible by the nonzero electric field component of the TM mode along the propagation direction y due to confinement [33], 2) Type I, where the pump photon is TM-polarized and the downconverted photons are both TE-polarized, 3) Type II, where the pump photon is TE-polarized and the downconverted photons are cross-polarized, one being TM, the other TE. In this paper, we focus on the Type II phase-matching which enables the direct generation of polarization-entangled photons.

B. Generated Quantum State and Polarization Entanglement

Experiments with Bragg reflection waveguides have been performed in both in the pulsed and continuous wave (CW) regime. For experiments in the pulsed regime we refer to the works done in the groups of A. Helmy and G. Weihs [35], [36]. In this paper we focus on experiments using a CW pump. In this case, the generated quantum state for a Type II phase-matching process, neglecting the generation of multiple pairs, can be written as [37]:

$$|\Psi\rangle_{\text{SPDC}} = \iint \mathrm{d}\omega_1 \mathrm{d}\omega_2 \mathcal{C}(\omega_1,\omega_2)\hat{a}^\dagger_H(\omega_1)\hat{a}^\dagger_V(\omega_2)|\text{vac}\rangle. \quad (3)$$

where $a^\dagger_\mu(\omega)$ denotes the creation operator of a photon at angular frequency ω and polarization $\mu = H, V$ and the complex function $\mathcal{C}(\omega_1,\omega_2)$ is the joint spectral amplitude (JSA), which is normalized to unity $\iint \mathrm{d}\omega_1 \mathrm{d}\omega_2 |\mathcal{C}(\omega_1,\omega_2)|^2 = 1$. The JSA, corresponding to the probability amplitude to measure one photon of a pair at ω_1 and its twin at ω_2, can be expressed as: $\mathcal{C}(\omega_1,\omega_2) = \alpha(\omega_1+\omega_2)\Phi_{\text{PM}}(\omega_p,\omega_1,\omega_2)\big|_{\omega_p=\omega_1+\omega_2}$, where $\alpha(\omega)$ is the pump spectrum and $\Phi_{\text{PM}}(\omega_p,\omega_1,\omega_2) = e^{-i\Delta k L/2}\text{sinc}(\Delta k L/2)$ is the phase-matching term where $\Delta k = k_p(\omega_p) - k_H(\omega_1) - k_V(\omega_2)$ is the wavevector mismatch. In order to evaluate Φ_{PM}, the effective mode indices of the guided modes involved in the downconversion process are calculated numerically using commercial electromagnetic simulation software suites relying on finite element methods. In Fig. 2(a), we show a simulation of the resulting joint spectral intensity JSI $= |\mathcal{C}(\omega_1,\omega_2)|^2$. We observe that the JSI presents strong frequency anticorrelations and that the two-photon emission spans a bandwidth of around 68 nm (8.5 THz), defined by the phase-matching function.

By rewriting the quantum state in the rotated basis: $\omega_+ = \omega_1 + \omega_2$ and $\omega_- = \omega_1 - \omega_2$, the JSA takes the product form [38]: $\mathcal{C}(\omega_1,\omega_2) = f_+(\omega_+)f_-(\omega_-)$ where the first term f_+ corresponds to the pump spectrum and the second term f_- to the phase-matching function.

Since the waveguide is pumped by a narrow-linewidth CW laser, one can approximate f_+ to a Dirac delta function centered on the pump laser angular frequency, $f_+(\omega_+) = \delta(\omega_+ - \omega_p)$, resulting in the following quantum state:

$$|\psi\rangle = \int_{-\infty}^{+\infty} \mathrm{d}\Omega \Phi(\Omega) a^\dagger_H(\omega_d+\Omega)a^\dagger_V(\omega_d-\Omega)|\text{vac}\rangle, \quad (4)$$

where we defined for convenience $\omega_d = \omega_p/2$ the degeneracy angular frequency, $\Omega = \omega_-/2$ the detuning with respect to the degeneracy and $\Phi(\Omega) = f_-(\omega_-)$ is the antidiagonal profile of the JSA. The modulus squared of the latter, extracted from the

simulation of Fig. 2(a), is shown in Fig. 2(b). The asymmetry of the JSI profile with respect to the degeneracy, indicated by a dashed line, stems from the intrinsic birefringence of the waveguide, as will be discussed in Section IV.

To show explicitly the presence of polarization entanglement, we rewrite the state as a continuous superposition of bipartite polarization-entangled states. This is done by splitting the integral in (4) into two parts using the identity $\int_{\infty}^{\infty} = \int_{0}^{\infty} - \int_{0}^{-\infty}$, then making the change of variable $\Omega \to -\Omega$ into the second term, and finally recombining the two integrals to obtain:

$$|\Psi\rangle = \int_0^{\infty} \mathrm{d}\Omega \left[\Phi(\Omega)|\omega_d + \Omega, H\rangle|\omega_d - \Omega, V\rangle + \Phi(-\Omega)|\omega_d + \Omega, V\rangle|\omega_d - \Omega, H\rangle\right], \quad (5)$$

where we defined for compactness: $|\omega, \mu\rangle = a_{\mu}^{\dagger}(\omega)|\mathrm{vac}\rangle$ with $\mu = H, V$. This expression corresponds to a continuous sum of polarization-entangled states distributed over the whole two-photon spectral bandwidth.

One of the crucial features of the device is that it emits photons that are inherently polarization-entangled at the chip output, without the need for off-chip temporal compensation. Indeed, the low birefringence of the waveguide and its small length imply that the temporal walk-off between H and V-polarized photons is negligible. This is an interesting advantage of the AlGaAs platform with respect to other types of sources based on birefringent crystals, such as type II ppLN waveguides [39], where walk-off compensation is necessary.

C. Generation of Biphoton Frequency Combs

Biphoton frequency combs are receiving growing attention in the integrated quantum photonics community due to their promising applications in quantum computing and communications protocols [40]. Important advances in this field have been achieved using hydex [41] or Silicon Nitride microrings [42], where four wave mixing is exploited to generate signal/idler photon pairs with a spectrum shaped by the microresonator resonances. In this context, the implementation of quantum optical microcombs generated via second-order nonlinear processes would lead to the advantages of higher brightness and avoid the spectral overlap of the pump beam with that of the biphoton state. A full description of the quantum state emitted by the integrated AlGaAs source has to take into account cavity effects arising from the nonzero reflectivity at the waveguide facets. Indeed, the index mismatch at the interface between the heterostructure and air induces a typical modal reflectivity of 0.27 (0.29) for fundamental TM (TE) modes. These values are calculated numerically using finite difference time domain methods. As a consequence, the waveguide can be modeled as a nonlinear $\chi^{(2)}$ medium surrounded by the two mirrors of an effective optical cavity. When photons are generated by SPDC, they bounce back and forth between the mirrors before exiting the system, as depicted schematically in Fig. 2(c). Conversely, in the spectral domain, the cavity effect implies that the downconverted photons cannot be generated at arbitrary frequencies but only at the discrete resonance frequencies of the cavity.

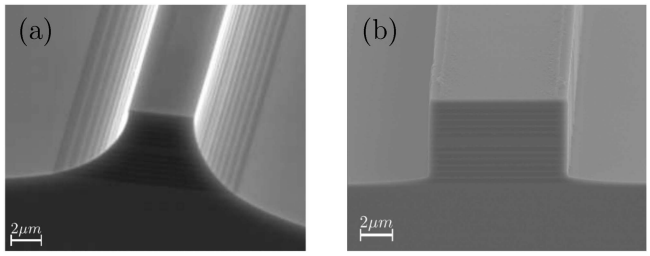

Fig. 3. Scanning electron microscope image of AlGaAs Bragg reflection waveguides fabricated using a (a) wet etching and (b) dry etching technique.

To describe this situation, we add an additional factor to the expression of the JSA. The JSA $\tilde{\mathcal{C}}(\omega_1, \omega_2)$ in the presence of a cavity can be expressed as [43]:

$$\tilde{\mathcal{C}}(\omega_1, \omega_2) = t_H(\omega_1) t_V(\omega_2) \mathcal{C}(\omega_1, \omega_2). \quad (6)$$

where the functions t_H, t_V are the amplitude transmission coefficients of H and V polarized light through the cavity: $t_{\mu}(\omega) = [(1 - R_{\mu})e^{i\omega\tau_{\mu}(\omega)/2}]/(1 - R_{\mu}e^{i\omega\tau_{\mu}(\omega)})$

with the round-trip time τ_{μ} defined as $\tau_{\mu}(\omega) = 2n_{\mu}(\omega)L/c$, where $n_{\mu}(\omega)$ and R_{μ} are respectively the effective mode index and modal reflectivity of the fundamental mode with $\mu = H, V$ polarization. Since the transmission function consists of a series of peaks, the product of the two cavity factors in (6) will result in a two-dimensional grid in frequency space. In Fig. 2(d), we show the antidiagonal profile $f_{-}(\omega_{-})$ experimentally reconstructed by stimulated emission tomography [44] exhibiting discrete resonance peaks, as described by the cavity terms in (6).

This property of the JSA demonstrates that the emitted state can be seen as a biphoton frequency comb (BFC), the quantum analog of an optical frequency comb. Taking a step further, we have also demonstrated that the symmetry of this state can be manipulated thanks to the interplay between cavity effects and temporal delay between photons of a pair [43], opening the way to new quantum protocols exploiting high-dimensional frequency states with controllable symmetry, such as the implementation of quantum logic gates [45], high-dimensional one-way quantum processing [46] or error correction in high-dimensional redundant states [34].

III. Waveguide Fabrication and Characterization

A. Cleanroom Fabrication and Measurement of Optical Losses

The AlGaAs waveguides are fabricated using two possible techniques. In the first method, the waveguides are patterned by photolithography then etched using a stoichiometric solution of $HBr/CH_3COOH/K_2Cr_2O_7$. The fabricated waveguide features smooth curvy sidewalls as illustrated in Fig. 3(a). This is the quickest and simplest method to fabricate an AlGaAs waveguide but its limited spatial resolution does not allow for complex designs. Nonetheless, the very low sidewall roughness leads to low propagation losses. This process has been used to fabricate standalone passive [47] as well as electrically driven photon pair sources [24].

The second fabrication method consists of an electron-beam lithography stage followed by a dry inductively coupled plasma (ICP) etching stage. The resulting ridge profile features upright sharp sidewalls, as can be seen in Fig. 3(b). This technological process allows for a higher spatial resolution enabling the fabrication of more complex monolithic chips combining several functionalities, such as two-photon sources and beam splitter [48].

The optical losses of the telecom modes supported by the fabricated devices are characterized using the method described in [49]. A telecom laser beam is focused on the input facet of the waveguide using a NA=0.95 microscope objective. Light at the output facet of the device is collected using an identical objective then directed to an infrared (IR) powermeter. The transmitted power is recorded while scanning the input laser wavelength λ. The transmissivity T, obtained by taking the ratio between the transmitted power and the input power of the laser, features a series of Fabry-Perot resonances. By measuring the contrast K of the Fabry-Perot fringes $K = (T_{\max} - T_{\min})/(T_{\max} + T_{\min})$ where $T_{\min}, T_{\max}$ are the maximum and minimum transmissivity, it is possible to obtain the combined loss-reflectivity coefficient $\tilde{R} = Re^{-\alpha L} = \frac{1}{K}(1 - \sqrt{1 - K^2})$. Using the numerically computed value for the modal reflectivity R, an estimate of the propagation losses can be found as $\alpha = \ln(R/\tilde{R})/L$.

The extracted values of the propagation losses for a 4 μm-wide wet etched waveguide are typically $0.3\,\mathrm{cm}^{-1}$ ($1.3\,\mathrm{dB\,cm}^{-1}$) and $0.5\,\mathrm{cm}^{-1}$ ($2.2\,\mathrm{dB\,cm}^{-1}$) for the fundamental TE and TM modes, respectively. In the case of a dry etched waveguide, these values are slightly higher: $0.5\,\mathrm{cm}^{-1}$ ($2.2\,\mathrm{dB\,cm}^{-1}$) for TE modes and $0.7\,\mathrm{cm}^{-1}$ ($3\,\mathrm{dB\,cm}^{-1}$) for TM modes respectively.

B. Pair Generation Rate and Coincidence-to-Accidental Ratio

In this section we assess the performance of our source in terms of pair generation rate (PGR) and coincidence-to-accidental ratio (CAR). In what follows, the PGR is defined as the number of generated pairs at the chip output per unit of internal pump power. These two figures of merit are measured by generating photon pairs by SPDC and recording time-correlation histograms of photon detection events. The experimental setup for this measurement is displayed in Fig. 5(b). The AlGaAs source is pumped with a tunable CW diode laser (TOPTICA TM Photonics DL pro 780) which is coupled into the waveguide through a microscope objective (NA = 0.95, 63×). Light emerging from the end facet of the waveguide is collected with a second identical microscope objective and sent to a fiber coupler, after filtering out the pump wavelength with a high pass filter. Temperature is kept constant with a heat sink stabilized with a Peltier cell and a thermistor in a PID loop. The photons are then split deterministically with a fibered polarizing beam splitter (FPBS) into two separate fibers and finally detected with superconducting nanowire single photon detectors (SNSPD, Quantum Opus) featuring a 85 % detection efficiency and 10 /s dark count rate. The time correlations between detector clicks are recorded with a time-to-digital converter (TDC, quTools) setting a temporal resolution of 162 ps.

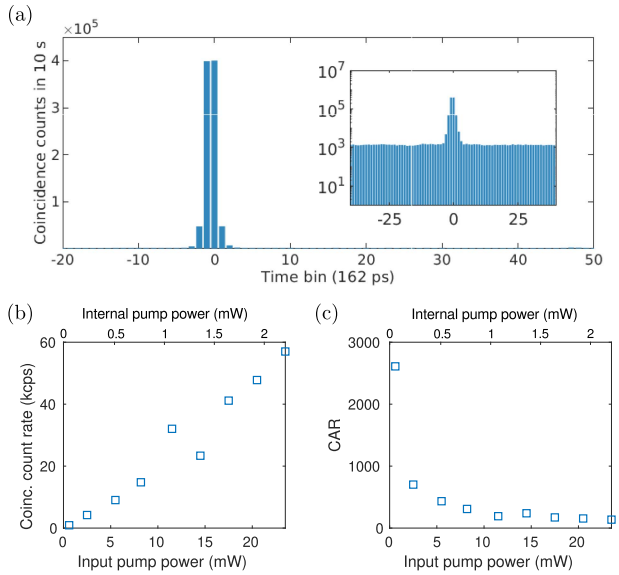

Fig. 4. (a) Experimental time-correlation histogram obtained for a pump power of 22 mW before the input microscope objective. The inset shows the data in logarithmic scale. (b) Measured raw coincidence count rate and (c) coincidence-to-accidental ratio (CAR) as a function of input pump power.

The result of the measurement is featured in Fig. 4. A typical time-correlation histogram is shown in Fig. 4(a) exhibiting a central coincidence peak which is the signature of simultaneous emission of the two photons of the pair. By integrating the number of counts in a time window of 6 temporal bins around the central peak, we extract the number C of raw coincidence counts. Similarly, we define the number of noise counts N as the total number of start-stop events within a different 6-bins window taken away from the coincidence peak. The coincidence to accidental ratio is then obtained as $\mathrm{CAR} = C/N$. Finally, we define the number of true coincidences as: $C_{\mathrm{net}} = C - N = C(1 - 1/\mathrm{CAR})$. In Fig. 4(b–c) we show the result of a measurement of C and CAR as a function of input pump power measured before the input microscope objective. The number of recorded coincidence counts grows linearly with pump power while the CAR is inversely proportional to the pump power. This is the usual behavior of SPDC sources operated in the low pump power regime, where the multiple pair emission events are negligible.

The PGR is deduced by taking into account the overall optical losses of the measurement setup to recover the number of pairs generated at the chip output. The PGR is defined as:

$$\mathrm{PGR} = \frac{C_{\mathrm{net}}}{\eta_A \eta_B \tau P_p^{int}} \tag{7}$$

where τ is the measurement integration time, P_p^{int} the internal pump power and η_A, η_B are the overall detection efficiency of the setup in the two detector paths A and B including the transmission coefficient of the sample and optical elements and the detectors quantum efficiency. The accurate estimation of η_A, η_B is done by inserting a variable attenuator before the

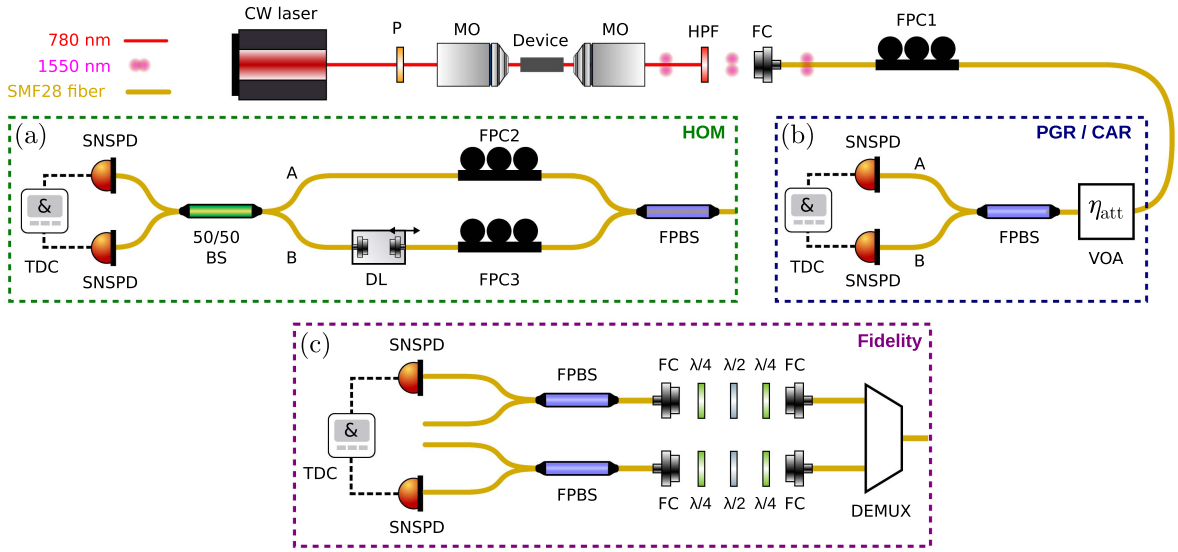

Fig. 5. Experimental setup for (a) Hong-Ou-Mandel interferometry, (b) measurement of the PGR and CAR, (c) measurement of the Bell state fidelity F. P: Polarizer, MO: Microscope Objective, HPF: High-Pass Filter, FC: Fiber Coupler, FPC: Fiber Polarization Controller, VOA: Variable Optical Attenuator, FPBS: Fiber Polarization Beam Splitter, SNSPD: Superconducting Nanowire Single Photon Detector, TDC: Time-to-Digital Converter, DL: Delay Line, 50/50 BS: 50/50 Beam Splitter, DEMUX: Demultiplexing device.

FPBS and recording the number of coincidences and single counts S_A and S_B as a function of applied attenuation α_{att}. The data are then fitted with the following expressions of C and S_A, S_B as a function of $\eta_{\text{att}} = 10^{-\alpha_{\text{att}}}$: $C = \eta_{\text{att}}^2 \eta_A \eta_B M$ and $S_{A(B)} = \eta_{\text{att}} \eta_{A(B)} M + d_{A(B)}$ where M is the total number of photon pairs generated by the source during τ and $d_{A(B)}$ are the dark counts of the detectors. We extract experimental values of $\eta_A = 11.8\,\%$ and $\eta_B = 11.7\,\%$. At maximum pump power $P = 22\,\text{mW}$, we record $C_{\text{net}} = 9.5 \times 10^4\,/\text{s}$ with a value of CAR of 80. By taking into account the transmission of the microscope objective (≈ 0.5) and the reflectivity of the facet for the Bragg pump mode (≈ 0.8), we estimate that $2\,\text{mW}$ of pump power are coupled inside the waveguide. Finally, the PGR for $1\,\text{mW}$ of internal pump power is $3.4 \times 10^6\,/\text{s/mW}$. This figure of merit will be used in Section IV-C to compare the performance of different platforms for integrated photon-pair sources.

IV. Broadband Indistinguishability and Polarization Entanglement

A. Characterization of the Biphoton State by Hong-Ou-Mandel Effect

Indistinguishable photons are a crucial resource for a large variety of quantum information protocols including long distance quantum communications [50], linear optical quantum computing [51], photonic boson sampling [52] and quantum metrology [53]. The Hong-Ou-Mandel (HOM) effect has become the reference testbench to probe the degree of indistinguishability between two photons [54], [55]. This effect occurs when two identical single-photons enter one in each input port of a 50/50 beam splitter. When the temporal overlap of the photons on the beam splitter is perfect, the two photons exit the beam splitter together in the same output mode, meaning that there is zero chance to get a coincidence event at the two output ports. The degree of indistinguishability between the photons of the pairs emitted by our device is tested by implementing the experimental setup depicted in Fig. 5(a). After being separated with a fibered polarizing beam splitter each photon enters one arm of an unbalanced interferometer, where one of the arms (arm b) features an optical delay line. Fibered polarization controllers in the two arms are used to align the polarization of the two photons. The two-photon wavepacket interferes on the final 50/50 beam splitter and time correlations are measured between the photons exiting the output arms. By recording the number of coincidences as a function of the applied time delay we extract the Hong-Ou-Mandel coincidence probability, which displays a dip around zero delay. Considering the quantum state of the source given in (3), we can calculate the HOM coincidence probability as [55]:

$$P_c = \frac{1}{2}\left[1 - \text{Re}\iint \text{d}\omega_1 \text{d}\omega_2 \mathcal{C}^\star(\omega_1, \omega_2)\mathcal{C}(\omega_2, \omega_1) e^{-i(\omega_1 - \omega_2)\tau}\right] \tag{8}$$

The visibility of the Hong-Ou-Mandel dip then reads:

$$V = 2\text{Re}\iint \text{d}\omega_1 \text{d}\omega_2 \mathcal{C}^\star(\omega_1, \omega_2)\mathcal{C}(\omega_2, \omega_1). \tag{9}$$

We see that V is directly proportional to the overlap integral between the JSA and its transpose. As a consequence, when the JSA is perfectly symmetric, corresponding to spectrally indistinguishable photons, the theoretical value of the visibility is 1. Any asymmetry in the JSA induces a decrease in the visibility. Therefore, V offers a direct readout of the degree of spectral indistinguishability between the two photons of the generated pairs.

In addition, the temporal width $\Delta\tau$ of the Hong-Ou-Mandel dip is inversely proportional to the biphoton bandwidth $\Delta\omega$. If we assume a Gaussian profile for the JSA, the HOM dip full

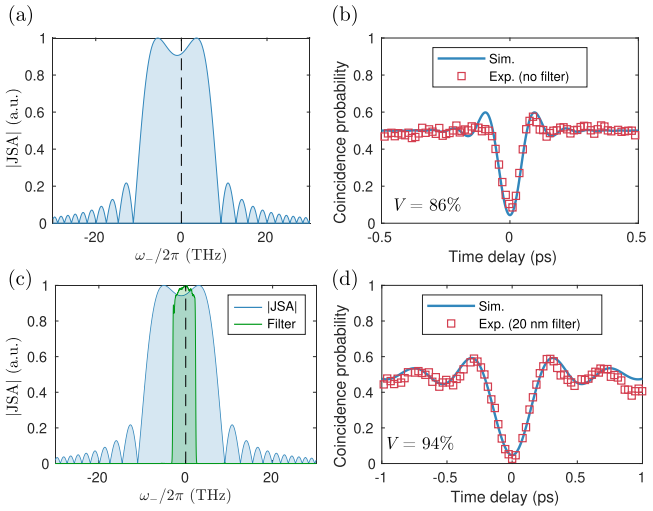

Fig. 6. Hong-Ou-Mandel interference. Simulated JSA modulus and experimental HOM interferograms in the case of (a-b) no filtering and (c-d) 20 nm square filter. The experimentally measured filter lineshape is represented as a green solid line in (c).

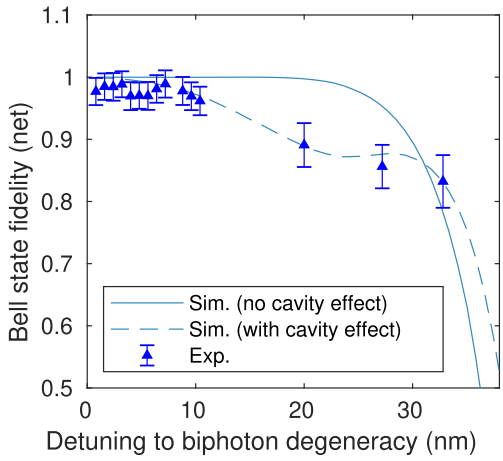

Fig. 7. Fidelity to the $|\Psi^+\rangle$ Bell state as a function of detuning to the biphoton degeneracy frequency. Errorbars are calculated assuming poissonian statistics.

width at half maximum (FWHM) is: $\Delta\tau = 1/(2\sqrt{2}\Delta\omega)$ [55]. The width of the dip can thus be related to the spectral bandwidth of the emitted two-photon state

The Hong-Ou-Mandel effect has been measured under two configurations: by sending in the HOM interferometer the full state produced by the AlGaAs device or by adding a 20 nm square filter before the FPBS centered at the degeneracy wavelength. Fig. 6 displays the experimental data and corresponding simulated JSA for each of these cases. In the unfiltered case, we obtain a HOM interferogram with a raw visibility of $86\,\%$ as can be seen in Fig. 6(b). The imperfect visibility can be explained by the fact that the simulated JSA, shown in Fig. 6(a), exhibits a slight asymmetry with respect to the value $\omega_- = 0$ (represented by a dashed line) which is a consequence of the small, yet nonzero, waveguide birefringence ($\Delta n = 7 \times 10^{-3}$). The FWHM of the dip is 83 fs corresponding to a state bandwidth of about 68 nm. When adding a 20 nm filter, we obtain a visibility of $94\,\%$ (Fig. 6(d)); indeed, in this case, the presence of the filter restores the symmetry of the biphoton spectral wavefunction, thus greatly reducing the effects of the residual birefringence. The dip FWHM in the filtered case is also higher, as expected, 267 fs which is compatible with the 20 nm bandwidth of the filter.

B. Broadband Polarization Entanglement

A number of recent works on entanglement-based quantum networks rely on broadband sources of polarization-entangled photon pairs, where the network capacity is directly proportional to the biphoton bandwidth [56], [57], [58]. As a consequence there is a growing interest towards the realization of chip-scale broadband sources of photon pairs [59], [60]. The effective bandwidth over which the generated photons are polarization-entangled is obtained by measuring a lower bound of the fidelity F to a $|\Psi^+\rangle$ Bell state, over the whole emission range of the chip. The experimental setup is depicted in Fig. 5(c). In this experiment, the generated signal and idler photons are separated into conjugate frequency channels using a demultiplexing device (demux), either a wavelength selective switch (Finisar 4000 s) or a coarse wavelength division multiplexing (CWDM, Fiber Solutions) module followed by a tunable filter (Alnair labs). Those channels are symmetrically distributed around the biphoton degeneracy frequency. Using two polarization analysis stages consisting of a set of $\lambda/2, \lambda/4, \lambda/2$ waveplates, a FPBS and a SNSPD, the polarization of the photons is projected onto the states of two mutually unbiased bases $\mathbb{Z} = \{|H\rangle, |V\rangle\}$ and $\mathbb{X} = \{|D\rangle, |A\rangle\}$ with $|D\rangle = (|H\rangle + |V\rangle)/\sqrt{2}, |A\rangle = (|H\rangle - |V\rangle)/\sqrt{2}$. By recording the number of coincidence counts between the two detectors in 8 different configurations : $C_{HH}, C_{HV}, C_{VH}, C_{VV}, C_{DD}, C_{DA}, C_{AD}, C_{AA}$ we can access the populations $\rho_{\mu\nu}$ of the density matrix in both bases: $\rho_{\mu\nu} = C_{\mu\nu}/(\sum_{\mathcal{B}} C_{\mu'\nu'})$ with $(\mu, \nu) \in \mathcal{B}$ and $\mathcal{B} \in \{\mathbb{X}, \mathbb{Z}\}$. Note that the normalization factor has to be calculated independently for the two bases. Finally a lower bound to F is obtained through the relation [61], [62]:

$$F \geq \frac{1}{2}\left(\rho_{HV} + \rho_{VH} - \rho_{HH} - \rho_{VV} + \rho_{DD} + \rho_{AA} - \rho_{DA} - \rho_{AD}\right). \tag{10}$$

The experimental results, along with the fidelity of the numerically simulated quantum state emitted by the AlGaAs chip, are shown in Fig. 7. We obtain a fidelity lower bound above $95\,\%$ ($85\,\%$) over a 26 nm (60 nm) spectral range.

We can see that the experimental points are well reproduced by a model including the cavity effects described in Section II-C, represented by a dashed line. These effects result in a faster decrease of the fidelity with detuning. This can be understood intuitively by considering that, due to birefringence and chromatic dispersion, the resonances of the cavity functions of (6) for TE and TM photons are not perfectly overlapping with respect to frequency degeneracy, resulting in extra asymmetries in specific regions of the JSA. This asymmetry corresponds to imperfect

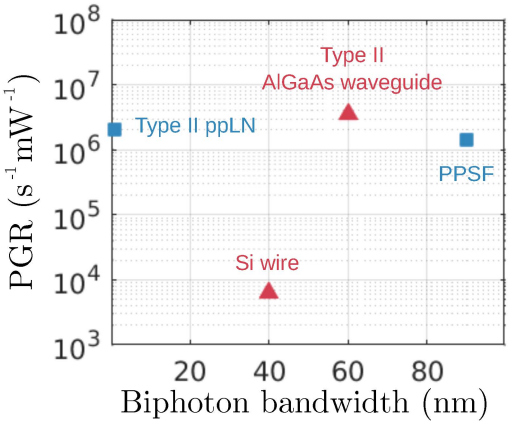

Fig. 8. Comparison between sources emitting broadband polarization-entangled photon-pair. Red triangles denote on-chip sources generating polarization entanglement directly at the chip output without additional optical elements. References: Type II ppLN [39], AlGaAs waveguide [58], Si Wire [63], PPSF [59].

photon indistinguishability leading to a decrease of the Bell state fidelity at large detunings. We emphasize that cavity effects can be eliminated by applying an antireflection coating on the waveguide facets. As a consequence, the simulation without cavity effects, denoted by a solid line in Fig. 7, predicts the upper bound on the achievable performance of our source, which could emit photon pairs with $F > 95\,\%$ over a spectral range of around 50 nm.

C. Comparison to Other Platforms

In this section, we compare the performance of the AlGaAs chip in terms of broadband polarization entanglement generation to state-of-the art sources in other material platforms: Si wire waveguides with integrated polarization rotators [63], Type II periodically poled lithium niobate (ppLN) waveguides [39] and periodically poled silica fibers (PPSF) [59]. ppLN, AlGaAs and Si are appealing platforms since the photons are generated on-chip and their quantum state can be manipulated by monolithic on-chip photonic circuits contrary to PPSF where the generated photons have to be re-coupled inside a separate chip to perform photonic gates. On the other hand, PPSF, AlGaAs and Si sources present the advantage of generating polarization-entangled photon pairs without the need of temporal walk-off compensation. On the contrary, Type II ppLN waveguides require an optical component, such as a polarization-maintaining fiber, to compensate for the group velocity mismatch between the two orthogonally polarized fields, which hinders direct generation of polarization entanglement at the chip output. Among the listed systems, AlGaAs waveguides and Si nanowires are the only two exhibiting both assets (on-chip integration and compensation-free generation).

Apart from these first two criteria, the quantitative figures of merit that are used to benchmark the different of photonic platforms are the biphoton bandwidth and the PGR. A graph displaying these quantities for all four platforms under consideration is shown in Fig. 8. We observe that PPSF, in addition to being a compensation-free source, has the highest biphoton bandwidth of 90 nm [59]. However, the AlGaAs waveguide source, on top of its compensation-free character and monolithic on-chip integration, has the highest PGR (3.4×10^6 /s/mW) in spite of a slightly smaller bandwidth of 64 nm. Based on these considerations, we conclude that AlGaAs Bragg-reflection waveguides are the only one of the four systems which is both suited for being used as standalone broadband direct polarization-entanglement sources as well as in monolithic and hybrid integrated photonic circuit architectures [48], [64].

V. Conclusion

In conclusion, we have presented a review on the generation of quantum states of light using AlGaAs Bragg reflection waveguides in a colinear modal phase-matching geometry. Exploiting the process of SPDC, these devices working at room temperature and compliant with electrical injection produce photon pairs in the telecom band, which can be entangled in different degrees of freedom. We have demonstrated a pair generation rate of the order of 10^6 /s/mW for a type II process and assessed the quantum purity of spectrally broadband states demonstrating a HOM visibility of 94% for a 20 nm-wide state and a fidelity above 95% to a polarization $|\psi^+\rangle$ Bell state over a spectral range of 50 nm. Many perspectives open up starting from these results. For example, the broadband polarization entanglement generated by the devices has recently been used as a resource to demonstrate a flexible entanglement-distribution network for secure communications in a laboratory experiment [58]. This result can be extended to develop new types of network topologies with an increased number of connected users as well as to contribute to the deployment of metropolitan quantum networks. The cavity effects present in our sample could also open the way to the utilization of the frequency degree of freedom for quantum information processing [34], [65] and to the combined exploitation of both polarization and frequency entanglement for future quantum networks. Finally, from the device development point of view, more functionalities can be added and implemented on-chip ranging from different types of beam splitters, to ultra-fast electro-optical phase control and hybrid integration with devices based on other platforms like photonic circuits in Silicon-On-Insulator or superconducting detectors [66], opening the way to the demonstration of large-scale photonic-circuit-based quantum operations.

References

[1] E. Pelucchi et al., "The potential and global outlook of integrated photonics for quantum technologies," *Nature Rev. Phys.*, vol. 4, pp. 194–208, 2022.
[2] A. Orieux, M. A. M. Versteegh, K. D. Jöns, and S. Ducci, "Semiconductor devices for entangled photon pair generation: A review," *Rep. Prog. Phys.*, vol. 80, no. 7, May 2017, Art. no. 076001.
[3] C. P. Dietrich, A. Fiore, M. G. Thompson, M. Kamp, and S. Höfling, "GaAs integrated quantum photonics: Towards compact and multi-functional quantum photonic integrated circuits," *Laser Photon. Rev.*, vol. 10, no. 6, pp. 857–857, 2016.
[4] C. Autebert et al., "Photon pair sources in AlGaAs: From electrical injection to quantum state engineering," *J. Modern Opt.*, vol. 62, no. 20, pp. 1739–1745, 2015.

[5] C. D. Watson, M. Poirier, J. M. Heaton, M. Lewis, and M. Boudreau, "Acoustooptic resonance in deep-etched GaAs-AlGaAs electrooptic modulators," *J. Lightw. Technol.*, vol. 22, no. 6, Jun. 2004, Art. no. 1598.

[6] J. Wang et al., "Gallium arsenide (GaAs) quantum photonic waveguide circuits," *Opt. Commun.*, vol. 327, pp. 49–55, 2014.

[7] W. Xie et al., "Ultrahigh-Q AlGaAs-on-insulator microresonators for integrated nonlinear photonics," *Opt. Exp.*, vol. 28, no. 22, pp. 32894–32906, Oct. 2020. [Online]. Available: http://opg.optica.org/oe/abstract.cfm?URI=oe-28-22-32894

[8] M. Pu, L. Ottaviano, E. Semenova, and K. Yvind, "Efficient frequency comb generation in AlGaAs-on-insulator," *Optica*, vol. 3, no. 8, pp. 823–826, Aug. 2016. [Online]. Available: http://opg.optica.org/optica/abstract.cfm?URI=optica-3-8-823

[9] T. J. Steiner et al., "Ultrabright entangled-photon-pair generation from an AlGaAs-on-insulator microring resonator," *PRX Quantum*, vol. 2, no. 1, 2021, Art. no. 010337.

[10] H. Mahmudlu, S. May, A. Angulo, M. Sorel, and M. Kues, "AlGaAs-on-insulator waveguide for highly efficient photon-pair generation via spontaneous four-wave mixing," *Opt. Lett.*, vol. 46, no. 5, pp. 1061–1064, Mar. 2021. [Online]. Available: http://opg.optica.org/ol/abstract.cfm?URI=ol-46-5-1061

[11] A. Helmy et al., "Recent advances in phase matching of second-order nonlinearities in monolithic semiconductor waveguides," *Laser Photon. Rev.*, vol. 5, 2011, Art. no. 272.

[12] A. Fiore, V. Berger, E. Rosencher, P. Bravetti, and J. Nagle, "Phase matching using an isotropic nonlinear optical material," *Nature*, vol. 391, no. 6666, pp. 463–466, 1998. [Online]. Available: https://doi.org/10.1038/35091

[13] L. Lanco et al., "Semiconductor waveguide source of counterpropagating twin photons," *Phys. Rev. Lett.*, vol. 97, Oct. 2006, Art. no. 173901. [Online]. Available: https://link.aps.org/doi/10.1103/PhysRevLett.97.173901

[14] S. Ducci, L. Lanco, V. Berger, A. De Rossi, V. Ortiz, and M. Calligaro, "Continuous-wave second-harmonic generation in modal phase matched semiconductor waveguides," *Appl. Phys. Lett.*, vol. 84, no. 16, pp. 2974–2976, 2004.

[15] M. Savanier et al., "Near-infrared optical parametric oscillator in a III-V semiconductor waveguide," *Appl. Phys. Lett.*, vol. 103, no. 26, 2013, Art. no. 261105. [Online]. Available: https://doi.org/10.1063/1.4853595

[16] S. Francesconi et al., "Engineering two-photon wavefunction and exchange statistics in a semiconductor chip," *Optica*, vol. 7, no. 4, pp. 316–322, Apr. 2020. [Online]. Available: http://opg.optica.org/optica/abstract.cfm?URI=optica-7-4-316

[17] S. Francesconi et al., "Anyonic two-photon statistics with a semiconductor chip," *ACS Photon.*, vol. 8, no. 9, pp. 2764–2769, 2021. [Online]. Available: https://doi.org/10.1021/acsphotonics.1c00901

[18] P. Yeh and A. Yariv, "Bragg reflection waveguides," *Opt. Commun.*, vol. 19, no. 3, pp. 427–430, Dec. 1976.

[19] A. S. Helmy, "Phase matching using Bragg reflection waveguides for monolithic nonlinear optics applications," *Opt. Exp.*, vol. 14, no. 3, pp. 1243–1252, Feb. 2006.

[20] C. Autebert et al., "Integrated AlGaAs source of highly indistinguishable and energy-time entangled photons," *Optica*, vol. 3, no. 2, pp. 143–146, Feb. 2016.

[21] P. Abolghasem and A. S. Helmy, "Single-sided Bragg reflection waveguides with multilayer core for monolithic semiconductor parametric devices," *J. Opt. Soc. Amer. B*, vol. 29, no. 6, pp. 1367–1375, Jun. 2012.

[22] A. Arjmand, P. Abolghasem, J. Han, and A. S. Helmy, "Interface modes for monolithic nonlinear photonics," *J. Opt. Soc. Amer. B*, vol. 32, no. 4, pp. 577–587, Apr. 2015.

[23] B. Pressl et al., "Semi-automatic engineering and tailoring of high-efficiency Bragg-reflection waveguide samples for quantum photonic applications," *Quantum Sci. Technol.*, vol. 3, 2018, Art. no. 024002.

[24] F. Boitier et al., "Electrically injected photon-pair source at room temperature," *Phys. Rev. Lett.*, vol. 112, May 2014, Art. no. 183901.

[25] O. Alibart et al., "Quantum photonics at telecom wavelengths based on lithium niobate waveguides," *J. Opt.*, vol. 18, no. 10, 2016, Art. no. 104001.

[26] S. Saravi, T. Pertsch, and F. Setzpfandt, "Lithium niobate on insulator: An emerging platform for integrated quantum photonics," *Adv. Opt. Mater.*, vol. 9, no. 22, 2021, Art. no. 2100789.

[27] S. K. Selvaraja et al., "Highly uniform and low-loss passive silicon photonics devices using a 300mm CMOS platform," in *Proc. Opt. Fiber Commun. Conf.*, 2014, Art. no. Th2A.33.

[28] D. Bonneau, J. W. Silverstone, and M. G. Thompson, *Silicon Quantum Photonics*. Berlin, Germany: Springer, 2016.

[29] J. F. Bauters et al., "Planar waveguides with less than 0.1 dB/m propagation loss fabricated with wafer bonding," *Opt. Exp.*, vol. 19, no. 24, pp. 24090–24101, Nov. 2011. [Online]. Available: http://opg.optica.org/oe/abstract.cfm?URI=oe-19-24-24090

[30] D. J. Blumenthal, R. Heideman, D. Geuzebroek, A. Leinse, and C. Roeloffzen, "Silicon nitride in silicon photonics," *Proc. IEEE*, vol. 106, no. 12, pp. 2209–2231, Dec. 2018.

[31] A. S. Helmy, B. Bijlani, and P. Abolghasem, "Phase matching in monolithic Bragg reflection waveguides," *Opt. Lett.*, vol. 32, no. 16, Aug. 2007, Art. no. 2399.

[32] A. Orieux, "Sources semiconductrices d'états à deux photons à température ambiante," Theses, Université Paris-Diderot - Paris VII, Dec. 2012.

[33] P. Abolghasem, J. Han, B. J. Bijlani, and A. S. Helmy, "Type-0 second order nonlinear interaction in monolithic waveguides of isotropic semiconductors," *Opt. Exp.*, vol. 18, no. 12, pp. 12681–12689, Jun. 2010.

[34] N. Fabre et al., "Generation of a time-frequency grid state with integrated biphoton frequency combs," *Phys. Rev. A*, vol. 102, Jul. 2020, Art. no. 012607.

[35] R. Horn, P. Abolghasem, B. J. Bijlani, D. Kang, A. S. Helmy, and G. Weihs, "Monolithic source of photon pairs," *Phys. Rev. Lett.*, vol. 108, Apr. 2012, Art. no. 153605.

[36] S. Auchter et al., "Understanding photoluminescence in semiconductor Bragg-reflection waveguides," *J. Opt.*, vol. 23, no. 3, Feb. 2021, Art. no. 035801.

[37] Z.-Y. J. Ou, *Multi-Photon Quantum Interference*. Berlin, Germany: Springer-Verlag, 2007.

[38] G. Boucher et al., "Toolbox for continuous-variable entanglement production and measurement using spontaneous parametric down-conversion," *Phys. Rev. A*, vol. 92, no. 2, Aug. 2015, Art. no. 023804.

[39] A. Martin et al., "A polarization entangled photon-pair source based on a type-II PPLN waveguide emitting at a telecom wavelength," *New J. Phys.*, vol. 12, no. 10, Oct. 2010, Art. no. 103005.

[40] M. Kues et al., "Quantum optical microcombs," *Nature Photon.*, vol. 13, no. 3, pp. 170–179, 2019. [Online]. Available: https://doi.org/10.1038/s41566-019-0363-0

[41] M. Kues et al., "On-chip generation of high-dimensional entangled quantum states and their coherent control," *Nature*, vol. 546, no. 7660, pp. 622–626, Jun. 2017.

[42] P. Imany et al., "50-GHz-spaced comb of high-dimensional frequency-bin entangled photons from an on-chip silicon nitride microresonator," *Opt. Exp.*, vol. 26, no. 2, pp. 1825–1840, Jan. 2018. [Online]. Available: http://opg.optica.org/oe/abstract.cfm?URI=oe-26-2-1825

[43] G. Maltese et al., "Generation and symmetry control of quantum frequency combs," *npj Quantum Inf.*, vol. 6, no. 1, 2020, Art. no. 13.

[44] M. Liscidini and J. E. Sipe, "Stimulated emission tomography," *Phys. Rev. Lett.*, vol. 111, no. 19, Nov. 2013, Art. no. 193602.

[45] P. Imany et al., "High-dimensional optical quantum logic in large operational spaces," *npj Quantum Inf.*, vol. 5, no. 1, 2019, Art. no. 59. [Online]. Available: https://doi.org/10.1038/s41534-019-0173-8

[46] C. Reimer et al., "High-dimensional one-way quantum processing implemented on D-level cluster states," *Nature Phys.*, vol. 15, no. 2, pp. 148–153, Dec. 2018.

[47] C. Autebert et al., "Integrated AlGaAs source of highly indistinguishable and energy-time entangled photons," *Optica*, vol. 3, no. 2, Feb. 2016, Art. no. 143.

[48] J. Belhassen et al., "On-chip III-V monolithic integration of heralded single photon sources and beamsplitters," *Appl. Phys. Lett.*, vol. 112, no. 7, Feb. 2018, Art. no. 071105.

[49] A. D. Rossi et al., "Measuring propagation loss in a multimode semiconductor waveguide," *J. Appl. Phys.*, vol. 97, no. 7, Apr. 2005, Art. no. 073105.

[50] H. de Riedmatten, I. Marcikic, W. Tittel, H. Zbinden, D. Collins, and N. Gisin, "Long distance quantum teleportation in a quantum relay configuration," *Phys. Rev. Lett.*, vol. 92, Jan. 2004, Art. no. 047904.

[51] E. Knill, R. Laflamme, and G. Milburn, "A scheme for efficient quantum computation with linear optics," *Nature*, vol. 409, pp. 46–52, 2001.

[52] D. J. Brod, E. F. Galvão, A. Crespi, R. Osellame, N. Spagnolo, and F. Sciarrino, "Photonic implementation of boson sampling: A review," *Adv. Photon.*, vol. 1, no. 3, pp. 1–14, 2019.

[53] E. Polino, M. Valeri, N. Spagnolo, and F. Sciarrino, "Photonic quantum metrology," *AVS Quantum Sci.*, vol. 2, no. 2, 2020, Art. no. 024703.

[54] C. K. Hong, Z. Y. Ou, and L. Mandel, "Measurement of subpicosecond time intervals between two photons by interference," *Phys. Rev. Lett.*, vol. 59, no. 18, pp. 2044–2046, Nov. 1987.

[55] K. Wang, "Quantum theory of two-photon wavepacket interference in a beamsplitter," *J. Phys. B: At. Mol. Opt. Phys.*, vol. 39, no. 18, pp. R293–R324, Sep. 2006.

[56] S. Wengerowsky, S. K. Joshi, F. Steinlechner, H. Hübel, and R. Ursin, "An entanglement-based wavelength-multiplexed quantum communication network," *Nature*, vol. 564, no. 7735, pp. 225–228, Dec. 2018.

[57] E. Y. Zhu, C. Corbari, A. Gladyshev, P. G. Kazansky, H.-K. Lo, and L. Qian, "Toward a reconfigurable quantum network enabled by a broadband entangled source," *J. Opt. Soc. Amer. B*, vol. 36, no. 3, Jan. 2019, Art. no. B1.

[58] F. Appas et al., "Flexible entanglement-distribution network with an AlGaAs chip for secure communications," *npj Quantum Inf.*, vol. 7, no. 1, Jul. 2021, Art. no. 118.

[59] C. Chen et al., "Compensation-free broadband entangled photon pair sources," *Opt. Exp.*, vol. 25, no. 19, Sep. 2017, Art. no. 22667.

[60] U. A. Javid, J. Ling, J. Staffa, M. Li, Y. He, and Q. Lin, "Ultrabroadband entangled photons on a nanophotonic chip," *Phys. Rev. Lett.*, vol. 127, Oct. 2021, Art. no. 183601.

[61] B. B. Blinov, D. L. Moehring, L.-M. Duan, and C. Monroe, "Observation of entanglement between a single trapped atom and a single photon," *Nature*, vol. 428, no. 6979, pp. 153–157, Mar. 2004.

[62] X.-Y. Chang, D.-L. Deng, X.-X. Yuan, P.-Y. Hou, Y.-Y. Huang, and L.-M. Duan, "Experimental realization of an entanglement access network and secure multi-party computation," *Sci. Rep.*, vol. 6, no. 1, Jul. 2016, Art. no. 29453.

[63] N. Matsuda et al., "A monolithically integrated polarization entangled photon pair source on a silicon chip," *Sci. Rep.*, vol. 2, no. 1, 2012, Art. no. 817.

[64] C. Agnesi et al., "Hong-Ou-Mandel interference between independent III-V on silicon waveguide integrated lasers," *Opt. Lett.*, vol. 44, no. 2, Jan. 2019, Art. no. 271.

[65] J. M. Lukens and P. Lougovski, "Frequency-encoded photonic qubits for scalable quantum information processing," *Optica*, vol. 4, no. 1, pp. 8–16, Jan. 2017.

[66] J. P. Sprengers et al., "Waveguide superconducting single-photon detectors for integrated quantum photonic circuits," *Appl. Phys. Lett.*, vol. 99, no. 18, 2011, Art. no. 181110. [Online]. Available: https://doi.org/10.1063/1.3657518